Simultaneous Adsorption and Incorporation of Sr^{2+} at the Barite (001) – Water Interface

Jacquelyn N. Bracco[1*], Sang Soo Lee[1], Joanne E. Stubbs[2], Peter J. Eng[2,3], Sarah Jindra[4], D. Morgan Warren[5], Anitha Kommu[6], Paul Fenter[1], James D. Kubicki[6], and Andrew G. Stack[7]

[1]Chemical Sciences and Engineering Division, Argonne National Laboratory, Argonne, IL, USA

[2]Center for Advanced Radiation Sources, University of Chicago, Chicago, IL, USA

[3]James Franck Institute, University of Chicago, Chicago, IL, USA

[4]Chemistry Department, Wright State University, Dayton, OH, USA

[5]Golder Associates Inc., Lakewood, CO, USA

[6]Department of Geological Sciences, University of Texas at El Paso, El Paso, TX, USA

[7]Chemical Sciences Division, Oak Ridge National Laboratory, Oak Ridge, TN, USA

[*]Corresponding Author: Phone (718)997-3338; email jacquelyn.bracco@qc.cuny.edu

[#]present address: Department of Earth and Environmental Sciences, Queens College, City University of New York, Flushing, New York, USA

Abstract

Ionically-bonded minerals are ubiquitous and play a determinative role in controlling the mobility of toxic metals in natural environments. However, little is known about the mechanism of ion uptake by these mineral surfaces. Here, the sorption of strontium ions (Sr^{2+}) to the barite (001) – water interface was studied using a combination of synchrotron x-ray scattering and three types of computational simulations (density functional theory, classical molecular dynamics (CMD), and CMD-metadynamics). In situ resonant anomalous X-ray reflectivity (RAXR) revealed that Sr^{2+} adsorbed on the barite surface as inner-sphere surface complexes and was incorporated within the outermost barite atomic layers. Density functional theory combined with classical molecular dynamics simulations confirmed the thermodynamic stability of these species, demonstrating almost equal magnitudes in the free energy of sorption between these species. Metadynamics simulations showed a more detailed feature in the free energy landscape for metal adsorption where adsorbed Sr^{2+} are stabilized in as many as four distinct inner-sphere sites and additional outer-sphere sites that are more diffuse and less energetically favorable than the inner-sphere sites. All three techniques confirmed Sr^{2+} adsorbs inner-sphere and binds to oxygens in the top two surface sulfate groups. The energy barriers among the inner-sphere sites were significantly lower compared with those for constituent cation Ba^{2+}, implying fast exchange among adsorbed Sr^{2+} species. The Sr^{2+} uptake measured by RAXR followed a Frumkin isotherm defined with an apparent free energy of sorption, $\Delta G_{Sr} \approx -22$ kJ/mol, and an effective attractive interaction constant, $\gamma \approx -4.5$ kJ/mol, between sorbed Sr^{2+}. While the observed free energy can be mostly explained by the Helmholtz free energy of adsorption for Sr^{2+}, $\Delta F_{Sr} = -15.3$ kJ/mol, the origin of the sorbate – sorbate correlation could not be fully described by our computational

work. Together, these experimental and computational results demonstrate the complexity of Sr^{2+} adsorption behavior at the barite (001) surface.

1. Introduction

Ion adsorption and exchange processes at mineral surfaces govern the fate of dissolved metal ions in the environment. These sorption processes depend on a variety of factors including, but not limited to, solution pH, the concentration and identity of the sorbate, the type of sorbent, surface functional groups on the sorbent, complexation of the sorbate and/or sorbent, and presence of other sorbates.[1] Ion hydration also strongly influences the strength and speciation of ion adsorption[2] with ions adsorbing as inner-sphere or outer-sphere complexes depending on the hydration state of the ion.[3] These sorption states can also be determined by the type of interaction with the mineral surfaces.[4-7] Ions adsorbed via electrostatic attraction can exist as a mixture of inner-sphere and outer-sphere complexes whose proportions are controlled mainly by the balance between electrostatic and ion-solvation energies,[4, 8-11] whereas ions adsorbed through strong covalent bonds form entirely inner-sphere complexes.[5] Ion adsorption to mineral surfaces can be described using different models with varying degrees of complexity. A subset of these models includes surface complexation models, such as the charge-distribution multi-site complexation (CD-MUSIC) model that incorporates surface protonation and bond valance theory.[12-14] Surface complexation modeling as applied to rutile has incorporated inner-sphere cation adsorption in addition to outer-sphere adsorption.[15-16]

Surface complexation models have also been applied to ionic mineral surfaces, but the extent to which such approaches are appropriate remains unclear. Ionic minerals, such as carbonate minerals, typically have higher reactivities in water than silicate or oxide minerals, which enables other mechanisms for ion-mineral reactivity than simple adsorption. For example,

surface complexation modeling of calcite ($CaCO_3$) suggests that the (104) surface can develop charge through protonation of carbonates or hydrolysis of water bound to calcium at the surface.[17-20] However, recent studies on the surface charge of calcite demonstrate that the (104) surface in circumneutral pH is nominally uncharged, consistent with recent observations that reveal negligible adsorption of monovalent Rb^+.[21] Similarly, there have been numerous studies of metal cation interaction with calcite, with results ranging from simple adsorption[22-25] to incorporation in the calcite structure through dissolution-reprecipitation mechanism (e.g., Pb^{2+} incorporation in the presence of EDTA).[26] This, along with results from molecular dynamics simulations and surface complexation modeling,[27] suggests that calcite reactivity may arise primarily from defect sites and surface topography.

Similarly, barite ($BaSO_4$) is well-suited to study how impurity ions interact with ionic mineral surfaces. Many studies unequivocally show the high reactivity of barite to impurity cations. Divalent ions are inferred to adsorb either as inner-sphere complexes to barite at concentrations > 10^{-3} M or as outer-sphere complexes at lower concentrations.[28] Sorption of calcium on barite was observed from batch uptake experiments and interpreted to occur as an outer-sphere ion.[29] In addition, strontium was also observed to readily sorb to barite step edges and other defect sites or incorporate into the crystal structure.[30-32] While process-based models have been shown to predict barite reactions under a wide range of solution conditions, atomic-level structural information on how metal ions adsorb onto or incorporate into barite surfaces is necessary to expand the models.

It is not known how the sorption of metal ions is controlled by the charge and structure of the barite surfaces. The dominant barite surface, barite (001), in barite-saturated solution is terminated by a stoichiometric mixture of barium and sulfate ions which are relaxed slightly

from their bulk lattice positions, leading to a surface that is nominally charge neutral.[33] The actual charge of the barite surface is, however, not well constrained. The (001) barite surface has been reported to carry a negative net charge in pure water at 25°C, possibly due to preferential retention of sulfate and release of barium ions from the surface,[34] yet it is unclear if surface charge develops in solutions saturated with respect to barite. Surface charge measurements of barite nanoparticles showed that the pH of the isoelectric point (pH_{iep}), where the surface is neutral, occurs around pH = 5 in sodium and calcium containing solutions.[35] However, Hang and coworker report that the pH_{iep} occurs around pH = 7.8 in deionized (DI) water spiked with NaOH.[28] Together, the wide range of behavior seen in these results suggests that the measured barite surface charges may not be intrinsic to barite but more likely arise from other factors, e.g., surface defects or local charge imbalance caused by impurity ion incorporation.

Recent computational works provide insight into the mechanistic understanding of metal adsorption to the barite surface. Adsorption of barium to barite (001) terraces has been found to be thermodynamically unfavorable based on computational simulations using a modified version of the GROMOS96 force field.[36-37] Subsequent metadynamics simulations, using a modified version of the MSXX force field,[38] found thermodynamically-favorable inner-sphere species adsorbed at a step edge developed on the barite (001) surface.[39] These two sets of computational simulations suggest the hypothesis that differences in the thermodynamic adsorption stability of divalent ions to steps and terraces on barite is central to understanding barite reactivity. However, direct experimental evidence has been lacking in these systems as a test of the various computational simulations.

In this paper, we demonstrate the first molecular-scale experimental and computational study of ion adsorption at the barite (001)-water interface. We resolve the sorption behavior of

strontium ions at the barite (001)-water interface using *in situ* specular crystal truncation rod (CTR) and resonant anomalous X-ray reflectivity (RAXR) measurements. The results are compared with density functional theory (DFT) and classical molecular dynamics (CMD) simulations to determine the positions and free energies of sorption for the strontium ions at the surface. The experiments were conducted over a range of dissolved Sr^{2+} concentrations: (3 to 225 μM) to determine uptake of strontium as a function of concentration. These results are compared with the adsorption behavior of divalent cations on charged (mica, rutile) and nominally uncharged (calcite) mineral surfaces.

2. Methods

2.1. Sample and Solution Preparation: Natural optically clear barite crystals from Sichuan, China containing minor trace impurities[40] were cleaved to expose the (001) surface. Samples were generally prismatic blades in shape, 5 mm thick, ~10 mm long along the longest axis, and 2.5-5 mm wide. Small particulate dust generated during the cleaving process was removed with compressed N_2 gas and DI water, and the cleaved sample was placed in a thin-film sample cell,[20, 41] which was then flushed with a barite saturated solution (BSS). The BSS was prepared by reacting barite powder with DI water on a shaker table for 3-4 weeks in the presence of atmospheric CO_2 and then filtered using a 0.1 μm pore membrane. The concentration of barium in this solution is ~ 10 μM.

Solutions containing strontium (Sr^{2+}) were prepared by adding $SrCl_2 \cdot 6H_2O$ to filtered BSS (pH ~ 5.6) immediately prior to injecting solution in the sample cell. All solutions were at saturation or slightly undersaturated with respect to barite, but undersaturated with respect to a $Ba_xSr_{1-x}SO_4$ phase. Approximately 1 mL of solution was injected in the cell for reaction with the crystal for 30 minutes, after which the excess solution was drained to form a thin film solution layer (~10 μm thick water layer at the surface held in place by an 8 μm-thick Kapton film (DuPont)) for X-ray measurements.[41] A Mylar hood containing humid helium was placed over the sample cell to limit evaporation of water through the Kapton film, which could increase the Sr^{2+} concentration in solution.[42] Additionally, solutions were flushed through the thin-film cell every 30 minutes to prevent increases in the strontium solution concentration with time due to water evaporation through the Kapton.[21] After flushing, the sample cell was puffed up and the crystal was reacted with the new solution for at least 30 minutes for re-equilibration. Four different samples were measured from the lowest to the highest strontium concentrations

(solution conditions available in Table S2). Two to three different spots on one sample were measured for each concentration to limit the effects of beam damage. For samples having variable surface roughness (e.g., characterized in XR data by a Robinson roughness parameter)[43] over the sample surface area, we typically observed variations in maximum strontium coverage, implying that presence of surface defects influences the strontium sorption density (Fig. S1 of the Supporting Information, SI). Despite this difference, fiducial measurements for all samples exhibited similar sorption behavior over both the strontium concentration range and reaction time, indicating that the sorption mechanism was the same for all samples even if the sorbed ion coverage was variable.

2.2. X-ray Reflectivity Measurements: Details of the setup for the CTR and RAXR measurements were described previously[33] and can also be found in SI. CTRs were collected in specular geometry as a function of momentum transfer, $Q = 4\pi \sin(\alpha_i)/\lambda$, (where λ is the X-ray wavelength and α_i is the incidence angle with respect to the surface) at a fixed energy (12 or 15 keV). The specular CTR was measured between $Q = 0.15 – 4.58$ Å^{-1} or $Q = 0.15 – 5.46$ Å^{-1} depending on the sample. RAXR measurements were made by scanning X-ray photon energy near the X-ray K absorption edge for Sr^{2+} ($E_0 \approx 16.1$ keV) at a series of fixed Q values. For each concentration of Sr^{2+} in solution, RAXR signals were measured at six or more distinct scattering conditions ($Q = 0.18$ to 1.54 Å^{-1}). We measured RAXR spectra repeatedly at $Q = 0.54$ Å^{-1} as a fiducial to monitor the sample stability during the measurement. Extended X-ray exposure to the sample led to decreases in both the overall reflectivity and the magnitude of the RAXR signal, the latter of which is indicative of X-ray induced desorption of strontium from the surface. Consequently, measurements were limited to two or three RAXR spectra for each spot on the

crystal before moving to a new spot which had not previously been exposed to X-rays in that solution condition.

2.3. CTR and RAXR Data Analysis: The CTRs were analyzed in the same manner as that of Bracco et al., 2017,[33] the details of which can be found in SI. RAXR spectra ($R(E,Q_o)$, i.e., the reflectivity as a function of photon energy at fixed Q) were analyzed in two ways. Initially, the individual RAXR spectra were analyzed in terms of a resonant structure factor defined by an amplitude ($A_R(Q)$) and a phase ($\Phi_R(Q)$) using a model-independent fitting algorithm.[44] The results from the model-independent fit were used to determine the initial parameters for fitting the data using a parametrized model that was optimized simultaneously for all RAXR spectra at a given condition. The energy-dependent anomalous dispersion terms f' and f'' were determined by measuring the X-ray absorption spectrum of 0.1 M $Sr(NO_3)_2$ solution in transmission mode and using a differential Kramers-Kronig transform.[45] The parameters for the CTR and RAXR fits were optimized using least-squares fitting using χ^2 ($= 1/N_p\Sigma_i(|R_i-R_c|/\sigma_i)^2$) as a goodness-of-fit where N_p is the number of data points, R_i and R_c are the measured and calculated intensities for the i^{th} data point, and σ_i is the measured uncertainty of the i^{th} data point.

2.4. Density Functional Theory (DFT): We performed DFT calculations with the program VASP [46-49] calculations on a periodic (001) barite surface to complement the X-ray scattering results. Model systems of 48 $BaSO_4$ + 195 H_2O and 48 $BaSO_4$ + 192 H_2O + Sr^{2+} + 2 Cl^- were constructed from the experimental crystal structure using the Surface Builder module of Materials Studio 2016 (Biovia Inc., San Diego, CA) with a 20 Å space between periodic slabs. The DFT calculation for Sr^{2+} adsorption to the barite surface was conducted using a model structure containing one Sr^{2+} in a solution volume of 17.768 × 16.374 × 20.000 $Å^3$. Further details are available in the supplemental information.

2.5. Classical Molecular Dynamics Simulations (CMD): CMD simulations were performed using a previously-developed force field for the barite-water system,[33, 50-51] combined with a modified set of parameters to account for strontium and its interaction with water.[52] Briefly, the force field is based on a simple point charge MSXX-style model[38] with flexible water (F3C),[53] but with simplified functional form of the short range interactions (Buckingham), along with more accurate hydration enthalpies of the aqueous ions.[50] Details of the force field and the simulations are shown in the Supporting Information.

A subset of the CMD simulations were designed to test the energy differences between the DFT and CMD simulations for strontium sorbed in various mechanisms. These CMD simulations used the DFT-optimized simulation cells as the starting point. They were performed using the MSXX force field, as described above, with either the flexible water model (F3C)[53] or the rigid point charge extended (SPC/E)[54] water model. There were five distinct DFT optimized starting configurations for the strontium ions: outer-sphere adsorbed, inner-sphere adsorbed, strontium-chloride ion pair adsorbed, strontium exchanged with one of the Ba_{high} ions (z = 0 Å) in the bulk, and strontium exchanged with one of the Ba_{low} ions (z = -1.1 Å) in the bulk.

2.6. Metadynamics Simulations: Adsorption of aqueous barium and strontium was probed by adding a single barium or strontium ion adsorbed to the (001) terrace in a bulk-like lattice position in a simulation cell containing 320 formula units of barite and 925 water molecules, with size of 34.4475 Å × 28.1422 Å × 57.2552 Å. Metadynamics,[55] specifically the PLUMED plugin[56] for LAMMPS,[57] was used to bias the sorbed ion. Due to the low symmetry of a surface site, three collective variables were used, its position in the *x*, *y*, and *z* directions. To prevent translation of the slab while biasing, the positions of six barium ions in the inner-most monolayer of barite were frozen at their average positions taken from an equilibration run. Gaussian-shaped

penalty potentials were added every 250 time-steps with a height of 0.4 kJ/mol and width of 0.1 Å. Well-tempered metadynamics was used to improve convergence with a bias factor of 20.[58] In order to improve sampling efficiency, the position of the biased atom was limited using exponentially-scaling external penalty potentials (walls). The width of the area that the atom was allowed to probe was 16 Å in the *x* and *y* directions, and ~13 Å in *z*. Multiple walkers were used to more efficiently sample the free energy landscape[59] using 30 different walkers. Altogether, approximately 400 ns of aggregate simulation time and 1.6 million hills were added for strontium, 300 ns and 1.2 million hills for barium. Hills were summed using the sum_hills software supplied by LAMMPS and put onto a 3D grid with a 0.1 Å spacing. Visualization was done with the VisIt software.[60] Free energy minima were evaluated for distinct adsorption positions and measured relative to the average energy of the hills added above 35 Å, above the outer-sphere adsorbed species.

3. Results

3.1. Effects of Sr^{2+} on Interfacial Structure: The structure of the barite-water interface as a function of Sr concentration is probed through high resolution CTR data (Figs. 1 and S2). The specular CTR signals in the presence of Sr^{2+} followed a similar pattern to those for the barite (001)-water interface (Fig. 1). Small but significant changes in the interfacial structure resulting from the presence of Sr^{2+} at the surface were most apparent in the midzones, particularly in $Q \approx 2 – 3$ and $Q \approx 4.5 – 4.7$ $Å^{-1}$. These differences are observed more easily after normalization of the CTR to the generic CTR shape[41] (Figure 1b). Changes in the shape of the CTRs can primarily be attributed to differences in intrinsic interfacial structures including the structure of the top-most barite monolayer and interfacial water because of the presence of Sr^{2+} as well as extrinsic factors such as sample roughness. No additional Bragg peaks, other than barite (00L) peaks, were

observed, indicating that there was no significant precipitation of any secondary phases (e.g., celestite, $SrSO_4$). This is consistent with the thermodynamics calculations that indicated the solutions were undersaturated with respect to any secondary minerals.

The CTR data with adsorbed Sr^{2+} were analyzed using the best fit model for the barite (001) CTR data in the absence of strontium[33] as a starting model ($\chi^2 \approx 19$ at $[Sr^{2+}] = 225$ μM). To accurately reproduce the intensity variations induced by the presence of strontium, the heights and occupancies of the ions in the top two monolayers and interfacial waters were allowed to vary. In these analyses, the composition in the model was assumed to be unchanged, and therefore changes in composition are reflected as effective changes in occupation factors. For example, substitution of Sr for Ba would be seen as a reduction of the apparent Ba occupation factor to the value Z_{Sr}/Z_{Ba}. The best fit models had quality of fits, χ^2, of 2.10 at $[Sr^{2+}] = 25$ μM, 3.42 at $[Sr^{2+}] = 75$ μM, and 1.05 at $[Sr^{2+}] = 225$ μM. For conciseness, the topmost and second topmost barium and sulfate ions are referred to as Ba_{high}, S_{high}, Ba_{low}, and S_{low}, respectively (Fig. S3). The best-fit models indicate that the observed differences in CTR data arose primarily through the displacements of the two topmost sulfate ions, a decrease in the apparent occupancy of Ba_{high} at $[Sr^{2+}] \geq 25$ μM, and changes in the amount and location of adsorbed species. The decreased occupancy of Ba_{high} is consistent with the exchange of Ba^{2+} at the surface by Sr^{2+}, which has a lower electron density. The total decrease in apparent electron density was 4.928 ± 0. 2 e^{-1} per A_{UC} at $[Sr^{2+}] = 25$ μM, 8.848 ± 0.3 e^{-1}/A_{UC} at $[Sr^{2+}] = 75$ μM, and 10.976 ± 0.2 e^{-1}/A_{UC} at $[Sr^{2+}] = 225$ μM, where A_{UC} (= 48.49 $Å^2$) is the area of the unit cell on the barite (001) surface. The number of bariums which would need to be fully replaced by strontiums to create this deficit in electron density corresponds to 27.4 ± 0.9 % of the Ba_{high} site at $[Sr^{2+}] = 25$ μM, 49.2 ± 1.6% at $[Sr^{2+}] = 75$ μM, and 61.0 ± 1.2% at $[Sr^{2+}] = 225$ μM (Table S3).

Vertical displacements of atoms in the topmost barite monolayer were more significant for the sulfate ions than barium ions. The S_{high} ions moved 0.14 ± 0.02 Å at $[Sr^{2+}]$ = 25 μM, 0.33 ± 0.02 Å at $[Sr^{2+}]$ = 75 μM, and 0.45 ± 0.03 Å at $[Sr^{2+}]$ = 225 μM, where positive values correspond to movement towards the solution. Displacements of S_{low} were -0.27 ± 0.02 Å at $[Sr^{2+}]$ = 25 μM, -0.20 ± 0.02 Å at $[Sr^{2+}]$ = 75 μM, and -0.23 ± 0.01 Å at $[Sr^{2+}]$ = 225 μM. Each of the top two bariums moved less than 0.04 Å in all three strontium concentrations. The displacement of sulfates at the surface led to increased corrugation of the surface at $[Sr^{2+}] \geq 25$ μM as compared to the absence of Sr^{2+}. Interestingly, the overall displacement of high and low sulfate groups suggests an expanding unit cell in the *z* direction as compared to the barite surface in the presence of BSS[33], which is contrary to the expected decrease in the size for the phase transition from barite with a longer lattice parameter (7.153 Å) to celestite with a shorter lattice parameter (6.867 Å).[61]

Changes in the solution electron-density profile (Fig. 2) were observed mostly within ~7 Å from the surface. The electron density of the first water adsorption layer at z ~ 2 Å increased at $[Sr^{2+}] \geq 25$ μM compared to the absence of strontium. At higher concentrations ($[Sr^{2+}] \geq 75$ μM), increased electron density was found ~ 1 Å above the surface, primarily from the displacement of S_{high}. The second adsorbed water layer, at *z* ~3.5 Å, shifted further from the surface and became broader and more electron-dense at higher Sr^{2+} concentrations. For all Sr^{2+} concentrations, the modulations in electron density damped out at *z* > 10 Å from the surface, above which the water structure became similar to bulk water.

3.2. Distribution of strontium at the surface: From the CTR results above, we can infer the presence of Sr^{2+} through its effects on the total electron density (Fig. 2). This behavior can be further explored through RAXR spectra that directly probe the presence of Sr^{2+} at the barite-

water interface as a function of Sr concentration (ranging from 3 to 225 μM). The RAXR spectra show little or no significant resonant modulations at Sr^{2+} concentrations of 3 – 18 μM (Figs. 3, S4-S16). This indicates that the amounts of Sr^{2+} present at the interface were small at these strontium concentrations. A sharp increase in RAXR amplitude was observed at $[Sr^{2+}]$ = 25 μM, above which the RAXR modulation amplitudes were mostly unchanged. At the same time, the shapes of RAXR spectra were mostly constant at the same Q, indicating that the distributions of Sr^{2+} sorbed at the interface were similar over this concentration range. The same trend was observed for all samples.

The magnitude and shape of the RAXR signals contain information on the amount and location of strontium at the surface, respectively. This information can be obtained using a model-independent approach wherein $F_R(Q) = A_R(Q)e^{[i\Phi_R(Q)]}$ where $A_R(Q)$ is the amplitude and $\Phi_R(Q)$ is the phase. The total strontium coverage can be estimated based on the amplitude at low Q and changes in the trend of the amplitude as a function of Q can be used to estimate the number of species of strontium (Fig. S17a). The average height of these species can be estimated based on the $\Phi_R(Q)/Q$ at low Q. As such, a change in the $\Phi_R(Q)/Q$ as a function of Q indicates there are multiple species present.

To obtain a more quantitative understanding of these data, we then compare the Q-dependent variation of the observed amplitude and phase values (Fig. S17) to the predictions of structural models. In this comparison, we find that the best fit model includes multiple strontium sorbed at the interface. For example, at $[Sr^{2+}]$ = 225 μM, the model-dependent RAXR analysis identified three sorbed strontium species: one located below the barite surface (z = -0.809 ± 0.084 Å), another adsorbed on the surface (z = 1.703 ±0.071 Å), and the third farther from the surface (z = 8.468 ± 0.577 Å). The sorption of the strontium below the surface implies

incorporation or exchange of strontium for barium in the top layer of the crystal lattice. From the CTR analysis, we observed that the occupancies of the barium in the top monolayer decreased with increasing strontium concentration. The exchange of more electron-dense barium with less electron-dense strontium results in the decrease of the overall electron density at the barium site. The location of this broad strontium species (-0.81 Å) is close to the average value of two barium planes (~ -0.65 Å), implying that the cation exchange occurred for both barium ions in the high and low positions. However, due to the finite resolution of the RAXR measurements (which was ~2 Å for the current datasets), we are unable to uniquely distinguish between one broadly-distributed, incorporated strontium species and two strontium species that replace the two topmost barium ions, although the latter is more chemically reasonable.

The second Sr^{2+} located at 1.70 Å above the surface can be interpreted as an inner-sphere complex adsorbed on the barite (001) surface because the height is too close to the surface to have intervening hydration layers. A simple way to determine if this height is physically possible is to estimate the bond distances between the adsorbed Sr and sites on the surface using a nearest neighbor analysis. The nearest neighbor analysis was conducted using the vertical surface atom positions (Ba_{high}, Ba_{low}, S_{low}, S_{high}) from the 225 μM CTR measurements (sample 1) and their lateral positions from our previous results in the absence of Sr.[33] This analysis demonstrates that Sr adsorbs in a location near the projected Ba_{low} ion site (i.e., if the crystal were extended by one monolayer) (Fig. 4) with an average Sr-O_s bond distance of 2.6 Å (2.6 for the nearest oxygen on S_{high} and 2.6 and for the nearest oxygen on S_{low}). Based on electrostatic interactions, it is more likely that strontium binds to these surface sulfate groups than bariums. For comparison, the measured strontium height is significantly lower than the heights of the water molecules adsorbed on the sulfate groups determined previously (2.41 and 3.52 Å),[33] indicating that

adsorbed strontium approaches the surface more closely and interacts more strongly with the surface groups than the water molecules. The third strontium species located far from the surface can be interpreted as an outer-sphere complex. However, the relative coverage of this species is low (<10%), indicating that the contribution of this species to the uptake of strontium to the barite surface is small. Further evaluation of the Sr adsorption positions is provided by the DFT calculations and CMD metadynamics simulations.

To determine how the strontium coverages changed with strontium concentration, all RAXR data collected in various strontium concentrations were analyzed based on the same structural model. In this analysis, the positions and rms widths of the three distinct strontium species were fixed while only the coverages were allowed to vary. The use of a smaller number of parameters effectively minimizes the covariance among the parameters especially for the datasets with fewer RAXR spectra. The analyses showed good agreement to all data (χ^2 = 1.08 – 2.00; Table S2), confirming the robustness of the approach.

The results revealed unusual behavior in the strontium uptake on the barite surface (Table S2, Fig. 5). At $[Sr^{2+}] \leq 18$ μM, only small amounts of strontium sorbed on the barite surface. With increasing $[Sr^{2+}]$ from 18 to 25 μM, the strontium coverage suddenly increased (by a factor of >5), and then quickly saturated at a constant strontium coverage up to $[Sr^{2+}]$ = 225 μM. This sudden increase cannot be explained by a simple adsorption model, i.e., using a Langmuir isotherm (Fig. 5), which implicitly assumes that an adsorbate behaves as an ideal gas and interacts with an adsorbent surface having a finite number of distinct adsorption sites. Instead, the observed trend can be expressed by a Frumkin isotherm, which takes into account the interaction between sorbates:

$$\theta_{Sr} = \frac{[\mathrm{Sr}^{2+}]\mathrm{K}_{ads}e^{\frac{-\gamma\theta_{Sr}}{RT}}}{1 + [\mathrm{Sr}^{2+}]\mathrm{K}_{ads}e^{\frac{-\gamma\theta_{Sr}}{RT}}}$$

where θ_{Sr} is the fractional coverage of strontium, K_{ads} is the apparent adsorption constant, and γ is the correlation energy. When the fractional coverage approaches zero, the Frumkin isotherm reduces to the Langmuir isotherm. From the best fit model, we obtained $K_{ads} = 10^{3.81 \pm 0.05}$ M^{-1}, which corresponds to the apparent free energy of adsorption, ΔG_{Sr}, of −21.8 ± 0.3 kJ/mol, and γ = −4.47 ± 0.21 kJ/mol. This correlation energy is negative, indicating an attractive sorbate-sorbate interaction.[63] The result indicates that the adsorption energy is increased by an effective attraction between the sorbates, leading to the sharp increase in the sorbed strontium coverage when $[Sr^{2+}] \geq 25$ μM (Fig. 5).

3.3. Density Functional Theory (DFT): The RAXR measurements, which demonstrate that Sr incorporates and adsorbs to the barite surface, can be considered as a starting point for the computational simulations. The DFT calculation for Sr^{2+} adsorption to the barite surface was conducted using a model structure containing one Sr^{2+} in a solution volume of 17.768 × 16.374 × 20.000 $Å^3$. In this calculation, the nominal Sr^{2+} concentration was ~0.01 M. This concentration, limited by the size of the model, is higher than the concentrations used for the X-ray measurements. The simulation time was also limited to 2.5 ps due to the size of the model and was used to assess migration of Sr^{2+} within a site. As such, the energies reported are potential energies from the minimization and should not be treated as absolute thermodynamic parameters.

The simulation results (Fig. 6 and S18) showed that adsorbed Sr^{2+} was stabilized at 2.2 ± 0.2 Å (Table S4, Figs. 6b, S18b), which is farther from the position of the adsorbed Sr^{2+} ion at *z* = 1.70 ± 0.07 Å from the X-ray results. To explore what might be leading to the differences in

adsorption heights for the DFT calculations and XR measurements, the distances of the inner-sphere adsorbed Sr from the different surface groups were measured. There are two surface ions within 3 Å of the Sr: an oxygen on S_{high} and an oxygen on S_{low}. Both species have an average Sr-O_s bond distance of 2.8 Å. For comparison, the bond distances for the XR results from the nearest neighbor analysis above are 2.6 Å. In addition, if a Sr is placed into the location expected from the DFT simulations above the XR derived surface, the height is very close to 1.7 Å. Together, these indicate that the height discrepancy is due to differences in the positions of atoms at the surface, rather than bond distances.

This confirms that while the apparent z heights for adsorbed Sr based on the RAXR measurements and DFT simulations may be different, the Sr^{2+}-O(S) bond distances are much more similar. The primary difference in the vertical heights instead arises from differences in the DFT and XR surface structures. In the CTR fits, the positions of Ba_{high}, Ba_{low}, S_{high}, and S_{low} are averaged over the entire surface. As such, a S_{low} group near an adsorbed Sr is assumed to have the same rotation and position as one which is not near an adsorbed Sr. The DFT simulations instead demonstrate that sulfate groups near the adsorbed Sr have a larger degree of rotation than those farther from the Sr. Additionally, the displacement of Ba_{high} and Ba_{low} at the surface depends on the proximity of these ions to the adsorbed Sr. This leads to a more corrugated surface than the one modelled in the XR measurements, as the XR measurements do not have the same individual ion sensitivity as the DFT calculations.

To check that the difference between the experimental and computational results was due to differences in surface structure rather than interactions with other ions, we tested the formation and adsorption of a Sr^{2+}–Cl^- ion pair based on the rationale that a weaker Sr^{2+}–Cl^- bond (compared to Sr^{2+}-O(H_2) bonds) would strengthen Sr^{2+} bonding to the surface O atoms (Fig.

S18d, S19-20). However, constraining the Sr^{2+} to ~1 Å above the surface with or without the Cl^- bonded resulted in much higher energies (> +40 kJ/mol) compared to the original inner-sphere adsorption. Furthermore, when the constraint on the Sr^{2+} was removed, the configuration reverted to a distance ~2.2 Å above the surface, confirming that the differences in the XR and DFT results is due to differences in the surface structure of the barite, rather than the strength of adsorption.

We also note that the outer-sphere model was +50 kJ/mol higher in energy than the inner-sphere model. This is consistent with the lower concentration of sorbed species in the outer-sphere model, but the DFT calculations may overestimate the energy difference because such a large ΔE would likely mean that no outer-sphere Sr^{2+} would be observed in the RAXR data. The higher energies may be due to un-relaxed solvation shells: That is, the residence time of water in the first solvation shell for aqueous barium is 208 ps[64] and those of various surface sites on the (001) barite surface range from 15-194 ps values.[51] These range of values are likely robust in that they are constrained by quasi-elastic neutron scattering measurements.[51] However, given the equilibration run of the DFT was shorter than these times at 100 ps, and the sorbed species were only run for 2.5 ps, it may be that the solvation shell of the sorbed species or the surface were trapped in a higher-energy, but metastable, state with a non-equilibrium number of water molecules.

We next tested the exchange of Sr^{2+} for Ba^{2+} in the Ba_{high} and Ba_{low} surface sites (Table S4 and Fig. S18). These Sr^{2+} exchange models in the high and low Ba^{2+} sites (Table S4, Figs. 6d, S18e and 6c, S18f) resulted in calculated energy changes (ΔE) of +8 and -6 kJ/mol, respectively, compared to the inner-sphere model. These ΔE values are small and within the level of uncertainties expected in our calculations. Thus, we conclude that the three positions for Sr^{2+}

have similar energies and rapid exchange would be possible if the energy barriers are relatively low. We did not investigate these exchange kinetics in this study, but modeling the potential mechanisms of exchange should be performed in the future. Our exchanged site positions range from -1.1 to 0.0 Å vertical displacement with respect to Ba_{high}. Combined with the model at 2.2 ± 0.2 Å, these three Sr^{2+} positions could give rise to the observed Sr density profiles obtained from RAXR spectra provided exchange is rapid compared to the experimental time scale (i.e., one site at z = -0.809 ± 0.084 Å and one at z = 1.703 ±0.071 Å).

3.4. CMD Simulations using the DFT Optimized Results: Potential energies for adsorbed Sr^{2+} were calculated using classical molecular dynamics simulations on the same models used for DFT-MD to provide a more detailed description of the site-specific stability of Sr^{2+} adsorbed on the barite (001)–water interface. Five distinct systems were investigated with Sr^{2+} exchange with Ba^{2+} in surface sites (both at the Ba_{high} and Ba_{low} surface sites), inner-sphere Sr^{2+} adsorbed on the surface with or without bonded Cl^-, and outer-sphere Sr^{2+}. Using both the F3C and SPC/E water models, we observed that the Sr^{2+} adsorbed as an inner-sphere complex has the lowest potential energy of all sorbed species considered (Table 2). The observation of a stable inner-sphere complex is consistent with DFT and RAXR results. However, the calculations show that Sr^{2+} exchanged for Ba^{2+} in the Ba_{high} and Ba_{low} sites are unstable compared with the inner-sphere Sr^{2+}. This is in stark contrast with the DFT results which show that the energies for the exchanged Sr^{2+} are similar to that for the inner-sphere Sr^{2+} (Tables 2 and S3). Finally, potential energies from both DFT and CMD simulations indicate that both the formation of a Sr^{2+}–Cl^- ion pair and adsorption of outer-sphere Sr^{2+} are energetically unfavorable at the barite–water interface (Table S4).

3.5. CMD Metadynamics: Although the DFT and CMD simulations provide results concerning the positions and relative energetics of ions adsorbed and incorporated at the surface, it has been well-documented that using solely potential energies does not capture absolute free energies and the activation energy barriers of transitions between distinct states.[52, 65-67] Here, metadynamics is used as an alternate method to reveal the free energy landscape and to provide more detail about the size and transitions between minima.

The free energy surfaces derived from the metadynamics for barium and strontium are shown in Figure 7. These two surfaces are quite similar, showing four distinct inner-sphere adsorption sites per A_{UC} (Fig. 7), along with a more diffuse and less energetically favorable series of outer-sphere positions. Similar to our previous results of water structuring at the barite-water interface, we observe a strong positional correlation with the surface functional groups.[33] Two of the inner-sphere species, IS_{low} and IS_{high}, coordinate S_{high}, though IS_{high} also coordinates S_{low}. These two species also adsorb in positions consistent with those of the bariums in the bulk crystal lattice, with IS_{low} adsorbing in the same position as the matching low barium and IS_{high} adsorbing in the same position as the matching high barium (Fig. S21). This suggests that these are coordinated to the barite surface in a manner similar to that found within the barite lattice. The second two inner-sphere species (IS_{NB}) are equivalent to one another, but do not adsorb in positions consistent with the crystal lattice. Both the adsorbed strontium and barium IS_{NB} species make one bond to a single surface sulfate (Fig. S21). Free energies of adsorption and adsorption heights for these two species are shown in Table 1. From this, we observe that the strontium is slightly closer to the surface than barium for the inner-sphere adsorbed positions. This is consistent with the relative sizes of the two ions (e.g., ion-water distances of 2.62 Å for strontium, 2.82 Å for barium[68]). For the free energies, we observe that the barium has a more

exothermic adsorption energy than strontium for all the inner-sphere bonding positions (e.g., -33.7 for barium vs. -15.3 kJ/mol for strontium adsorbed in the IS_{low} position), yet the outer-sphere adsorption energies are similar. The inner-sphere adsorption energies are consistent with the relative hydration enthalpies of strontium (-1443 kJ/mol)[68] and barium (-1305 kJ/mol)[68] to which the model was calibrated. This is rationalized in that the more strongly hydrated ion adsorbs less strongly because of the increased cost of dehydrating the adsorbing ion. Beyond the absolute magnitudes of sorption energies, the differences in the free energies between different states are smaller for strontium than for barium. This is also evident from the more contiguous free energy isosurfaces displayed in Figure 7, i.e., the minima for the strontium IS_{low} and the two IS_{NB} species are well-connected whereas for barium these are more distinct. This indicates that the activation energies for conversion between different adsorbed species states are lower for strontium than for barium, suggesting a more fluid and dynamic adsorption for strontium whereas barium is less reversible. Lastly, the relative free energy of adsorption for different states varies between strontium and barium. On barium all of the inner-sphere bound states with one bond to the surface (IS_{high}, IS_{NB}) have similar adsorption energies, but for strontium the IS_{high} site is not as preferred as the IS_{NB} sites. This may have implications for shifts in mechanisms that have been observed during crystal growth as the ratio of aqueous [Sr]/[Ba] is increased.[32]

4. Discussion

4.1. Strontium sorption behavior at the barite (001) surface: Based on the RAXR measurements, strontium present at the barite (001) surface exists as mixture of incorporated, inner-sphere adsorbed, and outer-sphere adsorbed species, with most of the adsorbed coverage in the incorporated and inner-sphere states. Evaluating these positions based on the computational simulations reveals the complexity of strontium interactions with the surface, particularly in the

case of the location of the incorporated species. Based on the DFT, CMD, and XR analyses, a probable inner-sphere adsorption site for a Sr ion is one near the position of a next-layer Ba_{low} ion if the crystal was extended, bonded to oxygens on S_{low} and S_{high}. Based on the results from the CTR measurements in the presence of strontium, we find a shift in the sulfate location upon Sr incorporation, where S_{high} moves towards the solution and S_{low} moves towards the bulk crystal, which could potentially indicate accommodation of strontium incorporation into a non-lattice position. However, the total displacements are too small – ranging from 0.14 Å up to a maximum displacement of 0.45 Å – to provide the space necessary for a strontium in an off-lattice position. Due to the finite resolution of the RAXR measurements, the best-fit model to the RAXR data is unable to distinguish between one broadly distributed incorporated strontium species at z = -0.809 Å from two strontium species that replace the two topmost barium ions at the surface at z = 0 and -1.1 Å. However, the DFT simulations indicate that exchange of strontium ions for Ba_{high} and Ba_{low} at the surface is energetically favorable. The CTR measurements are consistent with the computational simulations as a significant reduction in the electron density is observed in the topmost monolayer of the barite surface, which can be modelled as a reduction in the occupancy of Ba_{high}. Since strontium is ~30% less electron dense than barium, replacement of barium by strontium would lead to an overall reduction in the electron density at the surface. Therefore, we can conclude that the incorporated strontium likely arises from exchange for barium in the topmost layer of the barite crystal lattice.

It is possible this incorporation arises from a dynamic dissolution and growth process. Dove and Czank[69] calculated barite dissolution rates to be on the order of $10^{-7.1}$ mol/m^2/s in deionized water at 30°C. Dissolution rates would be expected to be much slower in the solutions utilized here, which were saturated or near saturation with respect to barite. However, while

attachment and detachment of surface ions is expected to be slow, it is not expected to be non-existent. In addition, the CTR analysis shows that the number of barium ions that would need to be replaced by strontium is systematically greater than the coverage of replacing strontium ions derived from the RAXR analysis (Table S3), suggesting that there can be some unfilled sites at the barite surface. This could result from dissolution of the surface, removing Ba, which then could be filled with a Ba, Sr, another type of ion, or left vacant. Adsorption of Sr could then compensate for the charge deficiency arising from vacancies.

4.2. Comparison of XR, DFT, and MD Simulations: There is overall good agreement between the computational simulations and experimental results. Both the RAXR results and computational simulations (DFT and CMD) indicate inner-sphere adsorption of strontium, and outer-sphere adsorption is found to be less favorable. The DFT simulations predict favorable exchange of strontium for bariums in the Ba_{high} and Ba_{low} lattice positions, while the RAXR results also indicate incorporation into the barite lattice. However, there are differences in the computational simulations and the experimental results, primarily in the height of the inner-sphere adsorbed species, although this height difference appears to be derived from differences in the barite surface structure rather than the location of Sr adsorption. The height of the adsorbed strontium ion from RAXR (~1.7 Å) was different from those from DFT, and CMD metadynamics simulations (2.2 Å, and 2.4 Å, respectively). To assess the statistical significance in these height differences, the RAXR data were fit using the positions of the computational simulations (Fig. S17). Fitting of the RAXR measurements was constrained to the incorporated (Ba_{low} and Ba_{high} heights from the DFT: z = -1.1 and 0 Å; rms-width = 0.1 Å) and adsorbed (z = 2.2 Å; rms-width = 0.5 Å) species. The DFT simulations could not determine the presence of outer-sphere Sr^{2+} mainly due to computational size limitations, but an outer-sphere adsorbed

species was included in the model fitting based on the RAXR data. The quality of fit for these positions was similar to the quality of fit for the unconstrained positions (i.e., ~10% difference in χ^2) despite the slight disagreement in the position in the center of mass for the inner-sphere species (Fig. S17b). The unconstrained RAXR model predicts slightly more (0.05 ± 0.01 Sr/A_{UC}) strontium adsorbed as an inner-sphere and slightly fewer (0.07 ± 0.01 Sr/A_{UC}) strontium incorporated than the model constrained by the DFT positions, but overall this confirms that the Sr inner-sphere adsorbed in the DFT simulations is likely the same one we are measuring using XR.

To evaluate the agreement between the CMD metadynamics simulations and the RAXR results, model fitting was constrained to the same incorporated species as the DFT simulations, since the CMD simulations were unable to probe incorporation, and three distinct adsorbed species predicted by the CMD simulations (IS_{low}, z = 2.4 Å, rms-width = 0.4 Å; IS_{high} and IS_{NB}, z = 3.5 Å, rms-width = 0.4 Å, and outer-sphere adsorbed, z = 6.3 Å, rms-width = 1 Å). The species predicted by the metadynamics simulations at z = 3.5 Å corresponds to three positions: the IS_{high} position and the two IS_{NB} positions, so these were condensed into the same species. The χ^2 value for this fit was ~30% higher than for the unconstrained RAXR model fit, indicating general agreement between the RAXR and CMD (Fig. S17c). When fitting the model using the CMD constrained positions, however, the best fit model converged to a model with no strontium adsorption at z = 3.5 Å, indicating that the CMD simulations overestimate the stability of Sr adsorbed in either the two IS_{NB} sites and/or the IS_{high} site. The amounts of strontium incorporated, inner-sphere adsorbed, and outer-sphere adsorbed were less similar for the CMD fit model and the unconstrained RAXR model than for the DFT fit model and the unconstrained RAXR model. The unconstrained RAXR model predicts greater inner-sphere coverage (by 0.1 ±

0.01 Sr/A_{UC}) and fewer incorporated (by 0.1 ± 0.01 Sr/A_{UC}) strontium coverages than the CMD fit model, which may contribute to the discrepancy between the goodness of fit as compared to the DFT model.

4.3. Strontium sorption energetics: One of the interesting features of the observed strontium adsorption/incorporation is that the behavior does not follow a simple Langmuir isotherm. The complex adsorption and incorporation behavior of strontium at the surface can instead be explained with a Frumkin isotherm. However, this behavior is not driven by either adsorption *or* incorporation behavior as the occupancies for the incorporated and adsorbed values are also unable to be independently fit to a Langmuir isotherm. The negative correlation constant (γ = -4.47 ± 0.021 kJ/mol) indicates there are effective attractive interactions between sorbates, i.e., strontium sorption to the surface drives additional strontium sorption. A potential explanation is that incorporation of a strontium makes subsequent adsorption of strontium more favorable. In the CMD simulations, the top layer of sulfate ions are fluxional, i.e. they rotate in place,[33] which, if true, could provide a mechanism for an adsorbed strontium exchanging with a barium ion at the surface (especially at a surface defect where exchange may take place with lower activation energy). Another suggestion is from the metadynamics results, which demonstrate that the strontium ions are more likely to convert between different adsorbed species on the surface than adsorbed barium ions (Figure 7).

To understand the energetics of Sr sorption on the barite surface, we compare the apparent free energy of sorption (ΔG_{Sr}) obtained from the isotherm measurement with the Helmholtz free adsorption energy (ΔF_{Sr}) of strontium from the metadynamics simulation. We first calculate the equilibrium constant for desorption from the IS_{low} site for strontium (K_{des} = $\exp(-\Delta F_{Sr}/RT)$, where R is the ideal gas) if we set the adsorbed species as the standard state with

activity = 1. This yields $K_{des} = 10^{-2.68}$ for strontium, within an order of magnitude of the concentration of desorption of barium in equilibrium with celestite ($10^{-3.32}$) (as a comparison, estimated $K_{des} = 10^{-5.82}$ for barium was also similar to that in equilibrium with barite in water, $10^{-4.97}$).[70] From this, the Helmholtz free energy for strontium adsorption was calculated to be ΔF_{Sr} = -15.3 kJ/mol relative to solution. This is somewhat smaller than but generally similar to the adsorption energy estimated from the RAXR measurement of ΔG_{Sr} = -21.8 ± 0.3 kJ/mol. This also confirmed that the magnitude of the adsorption energy for the IS_{low} position is fairly reasonable in the CMD model. However, this comparison cannot explain the sorbate–sorbate correlation energy observed from the isotherm measurements. Whatever aspects of the barite–solution interface that lead to a need for an effective sorbate–sorbate attractions characteristic of the Frumkin isotherm are likely not incorporated in these calculations and may be a larger source of error.

4.4. Differences in sorption behavior compared to other minerals: Based on the RAXR measurements, we find that strontium sorbs onto the barite surface through multiple sorption modes, including incorporation into the top $BaSO_4$ layer in the crystal lattice, and adsorption on the barite surface as both inner-sphere and outer-sphere species. Coexistence of inner-sphere and outer-sphere adsorbed species has been reported on a number of different mineral surfaces, including mica,[7] hematite,[8-9] corundum,[8] and quartz.[10] However, the observed coexistence of adsorbed and exchanged strontium is distinct from adsorption of ions at many other rock-forming mineral surfaces. On the muscovite (001) surface, cation adsorption occurs by electrostatic attraction to the negatively charged surface. On the calcite (104) surface, which is nominally neutral at circumneutral pH, ion sorption occurs though a range of mechanisms, including simple adsorption,[22-25, 71] incorporation (e.g., Pb substituting for Ca[26] or arsenate

incorporated in the crystal defects[72]), and precipitation (e.g., formation of epitaxial films[73]). On barite, incorporation is limited to the topmost portion of the barite surface. The best fit models using the DFT positions reveal that while strontium can incorporate into the Ba_{low} site in the barite lattice, approximately twice as much incorporation occurs at the Ba_{high} site. Additionally, there is a maximum amount of strontium which can adsorb to or incorporate into the surface, though there is sample-to-sample variation in the total amount (additional discussion available in the SI).

One main driving force for ion adsorption on mineral surfaces is electrostatic attraction. For the inner-sphere adsorbed species, we observed a maximum coverage of approximately 1 Sr^{2+} per every 3.3 unit cells (0.312 Sr^{2+}/A_{UC}), which corresponds to ~ 0.644 Sr^{2+}/nm^2. This would correspond to a surface charge of ~ -0.13 C/m^2 if adsorption was controlled by charge compensation. Adsorption driven through development of a negative charge on the barite surface could occur if the bariums have been hydrolyzed, but this is unlikely, based on results from Dove and Czank[69] and the pK_a for hydroxylation of the first solvation shell of aqueous barium (13.47).[74] It could also result from a portion of the bariums being removed from the surface and not being fully replaced by strontium ions, creating unfilled sites at the surface. A comparison of the amount of bariums that would need to be replaced based on the CTR results to the actual measured incorporated strontium based on the RAXR results (Table S3) suggests it is likely there are some unfilled sites at the barite surface. The sample-to-sample variation in strontium adsorption suggests that the adsorption behavior is not driven through electrostatic attraction due to an intrinsic surface charge since the samples were all measured at approximately the same pH. As such, the terraces of the different samples would be expected to have the same or similar surface charge. Inner-sphere adsorption has been reported for monovalent, divalent, and trivalent

ion adsorption on the charged rutile (110) surface, but this is associated with the attractive interaction driven by the pH-dependent surface charge of the surface oxygen sites that also serve to complete the first coordination shell of the partially-dehydrated sorbed cations.[14] While in our experiments, the barite surface is likely uncharged, in the metadynamics simulations the topmost sulfates are rotated (Fig. S21) to complete the first coordination shell of the inner-sphere adsorbed strontium ions. This is similar to prior simulations of barium adsorption onto barite, where the sorbed barium (partially coordinated by the surface sulfate groups) was found to be under-coordinated, and the type of site to which the barium was adsorbed played a role in precisely how many waters were lost.[50] For example, for a barium adsorbed in the Ba_{low} bulk-like position, the coordination number was found to be ~6 (relative to 8.1 in aqueous solution), but proportionally gains three bonds to oxygens on sulfate. However, bariums adsorbed in the Ba_{high} bulk-like position were under-coordinated and lost an additional two waters, but with no difference in the coordination number to oxygens on sulfate to the Ba_{low} species. For strontium in this study, the coordination number of the aqueous species is 8.3, but adsorbed in the Ba_{low} bulk-like position, its coordination number is ~6.8, a loss of ~1.5 waters. Thus the details of the solvation structures of the surface and sorbed species may be influencing the adsorption behavior and the fraction of the hydration shell that is retained by the sorbed species.

Exchange of Sr^{2+} for Ba^{2+} in the barite surface is expected given the similarity of size and chemical property between two cations. A similar phenomenon has been observed for calcite equilibrated in solutions containing Pb^{2+} in the presence of EDTA.[26] In this experiment, the amount of Pb^{2+} incorporates up to four layers into the calcite crystal, with decreasing Pb^{2+} incorporating with depth and minimal surface adsorption. The authors attribute these results to a dissolution-reprecipitation mechanism in which the amount of Pb^{2+} in each layer decreases due

to a decrease in the fraction of subsurface layers exposed. The authors also present evidence that Pb^{2+} does not adsorb to a calcite surface in the absence of EDTA, indicating that the dissolution-reprecipitation mechanism occurring at steps exposed via etch pit formation is what is driving Pb^{2+} incorporation into the surface. Incorporation of radium into the barite crystal lattice has also been observed in excess of what would be predicted thermodynamically, which also occurs via a dissolution-reprecipitation mechanism.[75] This is a significantly different situation than the results presented here – in our case the barite surface is in solutions at or very near equilibrium. This may occur due to the relative size differences in Pb/Ca or Ra/Ba and Sr/Ba as Ra^{2+} is larger than Ba^{2+}, Pb^{2+} is larger than Ca^{2+}, and the $PbCO_3$ crystal structure differs from that of calcite while Sr^{2+} is smaller than Ba^{2+} but the crystal structures for barite and $SrSO_4$ are the same.

5. Summary and Conclusions

The sorption of Sr^{2+} on the barite (001) surface was investigated using a combination of synchrotron X-ray scattering and computational simulations. Together, these results demonstrate that strontium both incorporates into and adsorbs to the barite (001) surface. The incorporated strontium most likely substitutes for the Ba_{low} and Ba_{high} ions in the surface (z = 0 and -1.3 Å), while the adsorbed strontium primarily forms inner-sphere complexes. The inner-sphere Sr likely adsorbs to oxygens in the S_{high} and S_{low} groups, near the position of a next-layer Ba_{low} ion if the crystal was extended. Results from the metadynamics simulations indicate that strontium adsorbs to barite surfaces less readily than barium, but the strontium that does adsorb to the surface migrates more readily between IS_{high}, IS_{low}, and IS_{NB} sites than barium ions. This implies there may be a larger energy barrier to strontium adsorption than barium adsorption. The RAXR measurements indicate a complex sorption behavior by strontium, in which strontium coverage is near zero at $[Sr^{2+}] < 18$ µM, but sharply increases and plateaus at $[Sr^{2+}] \geq 25$ µM. This uptake

behavior follows a Frumkin isotherm defined with an apparent free energy of sorption, $\Delta G_{Sr} \approx -22$ kJ/mol, and an effective attractive interaction constant, $\gamma \approx -4.5$ kJ/mol, between sorbed Sr^{2+}. While the observed free energy can be largely explained by the Helmholtz free energy of adsorption for Sr^{2+}, $\Delta F_{Sr} = -15.3$ kJ/mol, derived from the metadynamics simulations, the origin of the sorbate – sorbate correlation could not fully described by our computational work. In the case of a large energy barrier limiting strontium adsorption to flat terrace regions, strontium may adsorb more readily to defects on the surface, such as kink sites. However, our CTR and RAXR results suggest that surface roughness does not play a significant role in the extent of strontium coverage at the surface. Further research comparing adsorption to and incorporation into barite surfaces with controlled defect and step densities would enable us to precisely determine the favorability of incorporation at steps as compared to terraces.

Supporting Information

Additional methods and discussion, Figures S1-S21, Tables S1-S4

Acknowledgements

This work was supported by the U.S. Department of Energy, Office of Science, Basic Energy Sciences, Chemical Sciences, Geosciences, and Biosciences Division. CTR measurements were performed at GeoSoilEnviroCARS (The University of Chicago, Sector 13), Advanced Photon Source (APS), Argonne National Laboratory. GeoSoilEnviroCARS is supported by the National Science Foundation - Earth Sciences (EAR-1634415) and Department of Energy- GeoSciences (DE-FG02-94ER14466). A subset of the RAXR measurements (sample 2) were measured at Sector 33-ID-D. This research used resources of the Advanced Photon Source, a U.S. Department of Energy (DOE) Office of Science User Facility operated for the DOE Office of Science by Argonne National Laboratory under Contract No. DE-AC02-06CH11357. Computational resources for the DFT and portions of the CMD simulations were provided by The Pennsylvania State University Institute for CyberScience, the NSF XSEDE program, and the University of Texas at El Paso Research and Academic Data Center. Metadynamics simulations were performed using the National Energy Research Scientific Computing Center (NERSC), a U.S. Department of Energy Office of Science User Facility operated under Contract

No. DE-AC02-05CH11231**.** The authors thank Dr. Musa Hussein and Amanda Labrado for assistance performing calculations and analysis of the results.

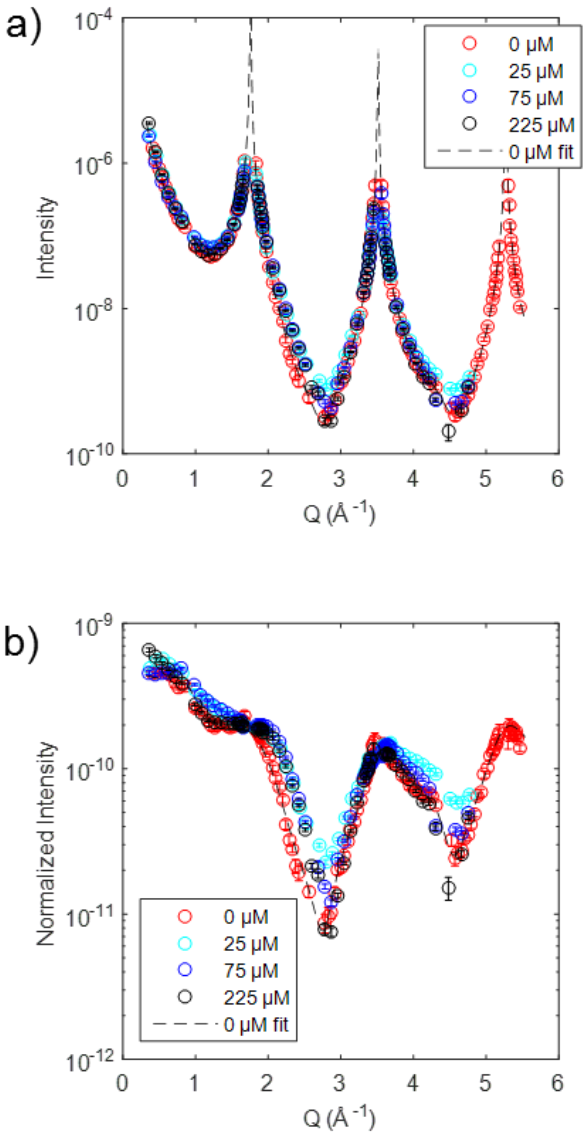

Figure 1. a) Specular CTRs and b) normalized CTRs for barite (001) collected in a 0-225 μM $SrCl_2$ solutions. The general shape of the CTRs is the same at all four concentrations, indicating the strontium does not significantly affect the interfacial structure. Small differences as a result of strontium adsorption/incorporation can be observed primarily between Q = 2 and 3 Å^{-1}.

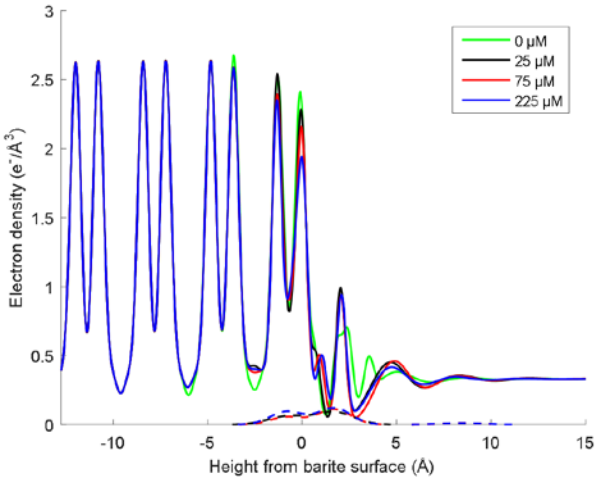

Figure 2. Electron density profiles in the presence of 0-225 µM Sr^{2+}. A decrease in the electron density occurs primarily in the top monolayer (consisting of the top two bariums and sulfates) of the surface with increasing strontium concentration. The areas encompassing the dashed lines are the Sr-specific electron density derived from the RAXR data fit.

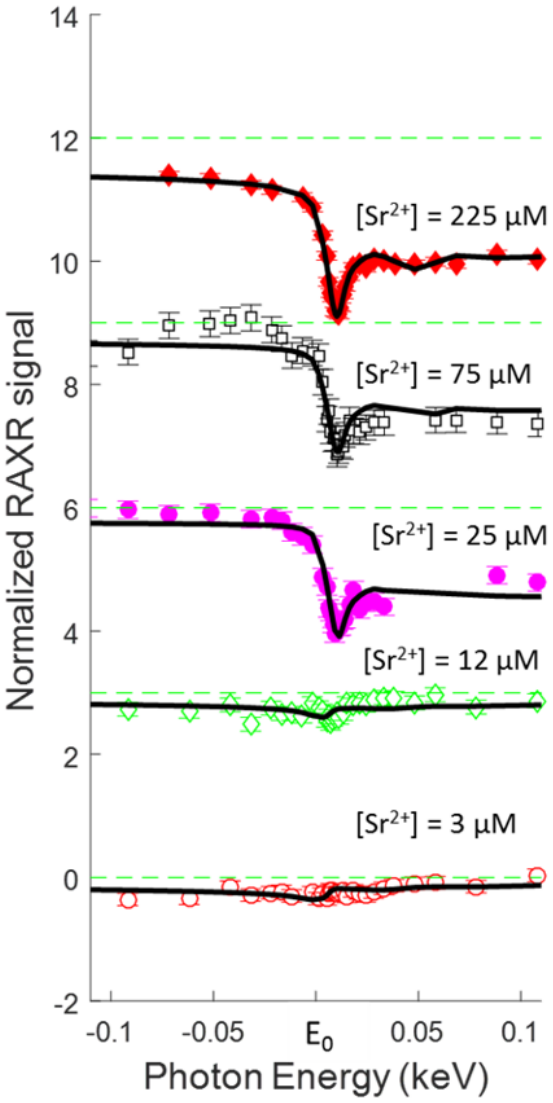

Figure 3. Normalized RAXR signals (using the resonant amplitude normalization $[|F_{tot}|^2 - |F_{NR}|^2]/2|F_{NR}|$, where F_{NR} is derived from the best-fit of the CTR data[62] near the K-absorption edge of Sr^{2+} plotted as a function of concentration at Q = 0.54 $Å^{-1}$. Black lines are derived from the best fit model to the data. Each spectrum is offset along the y-axis for visual comparison (see the green dotted lines). No modulation in the RAXR signal would be expected in the absence of strontium. The full datasets and best-fits can be found in Figs. S4-16 in the SI.

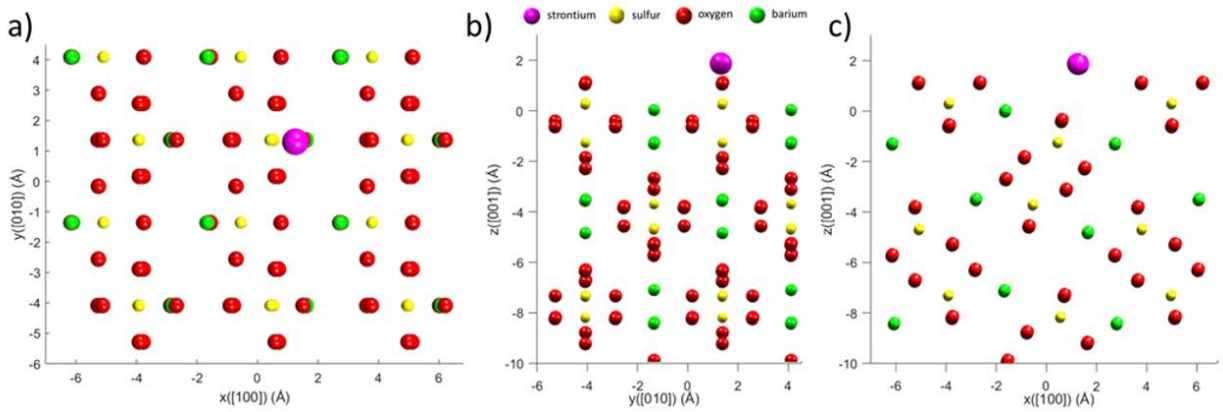

Figure 4. Views along (a) [001], (b) [010], and (c) [100] of inner-sphere Sr adsorption to the barite (001) surface based on the nearest neighbor analysis of the XR measurements. The results suggest that inner-sphere Sr adsorbs in a site near the projected Ba_{low} position if the crystal was extended by one layer.

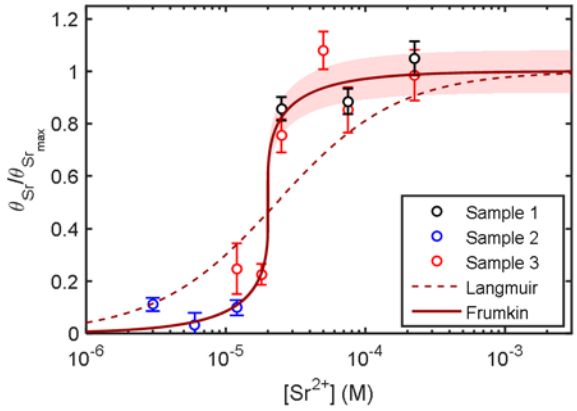

Figure 5. Normalized occupancy of adsorbed and incorporated strontium plotted as a function of concentration of strontium in solution. Occupancies were derived from the model fits to the RAXR spectra for each data point. A Frumkin isotherm (solid line) fit the data significantly better than a Langmuir isotherm (dashed line). The light red shaded region corresponds to the 1-sigma uncertainty in the normalized strontium occupancy for the Frumkin isotherm.

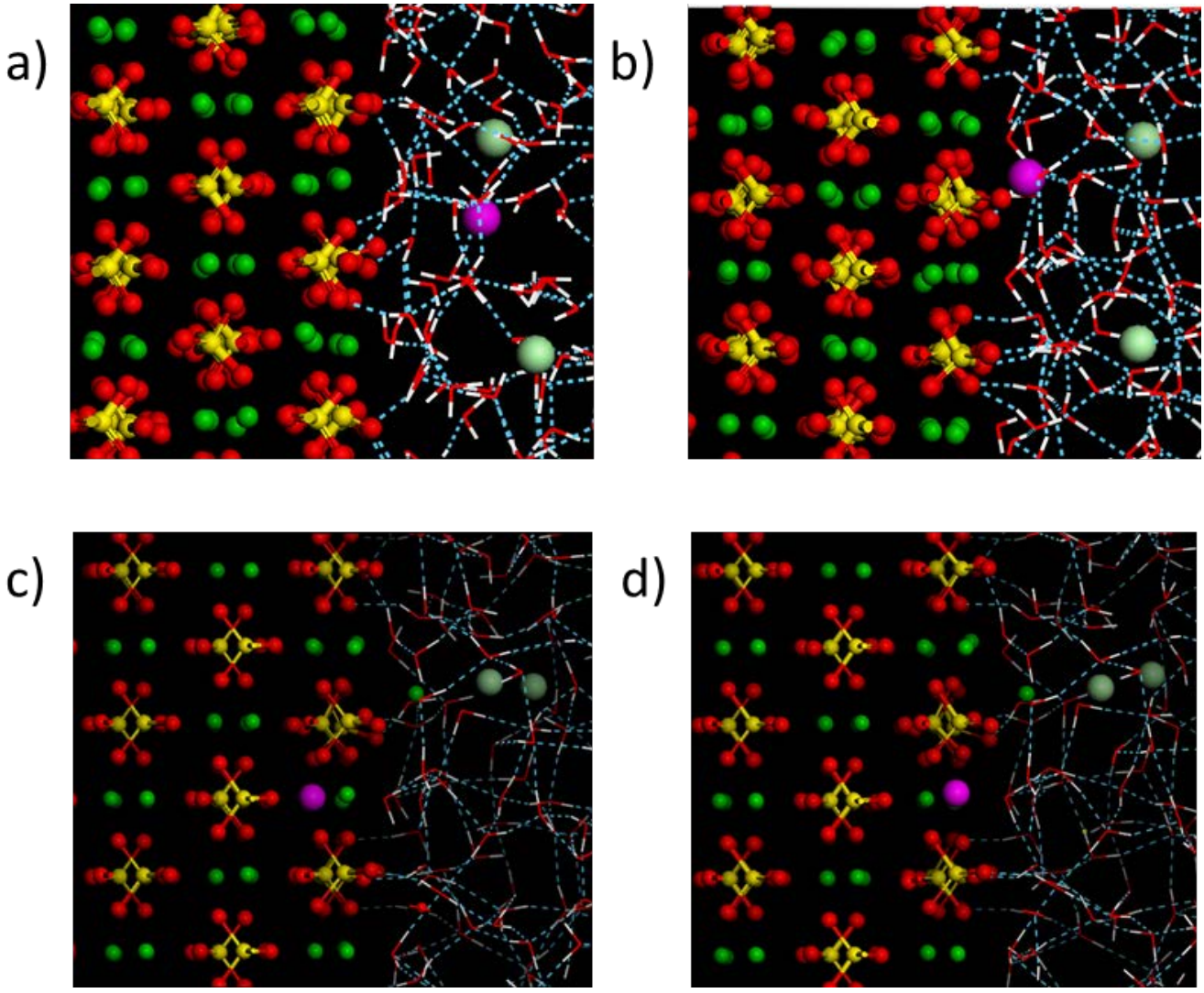

Figure 6. Close-ups of configurations used in the DFT and DFT optimized CMD simulations of (a) outer-sphere, (b) inner-sphere, exchanged (c) Ba_{low} site, and (d) Ba_{high} site $SrCl_2$-barite-water. Views are roughly along the [100] axis. O red, H white, Ba green, S yellow, Sr pink, Cl light green. Full sized views are available in the supporting documentation (S18).

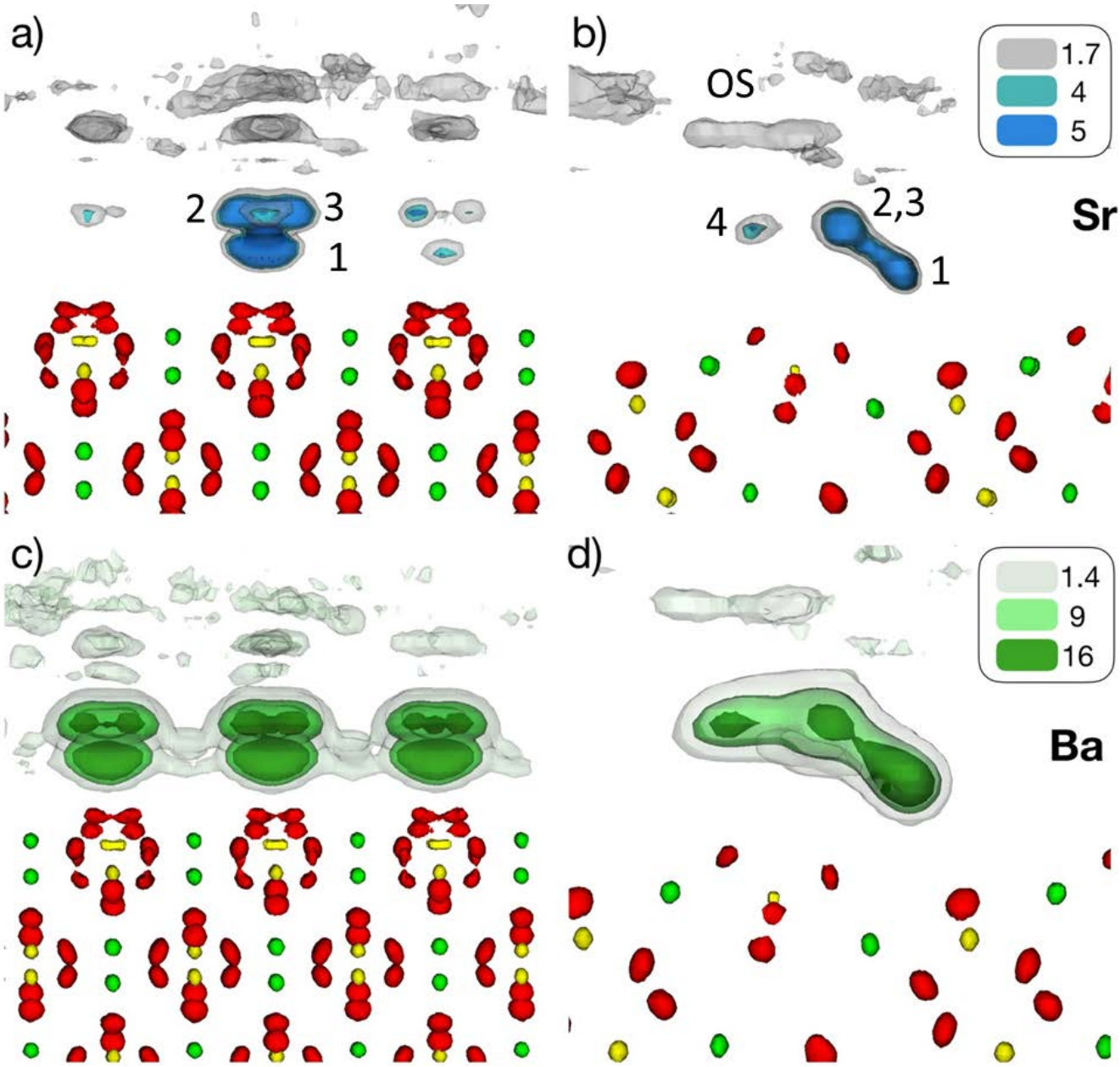

Figure 7.: Free energy isosurfaces for adsorption of strontium (a, b), and barium (c, d). Views along the [100] (a, c) and [010] (b, d) directions of barite are shown. The absolute minimum for strontium adsorption was -15.3 kJ/mol, whereas for barium it was -33.2 kJ/mol. Site 1 (labelled in b) corresponds to the IS_{low} species, sites 2 and 3 corresponds to the IS_{NB}, site 4 corresponds to the IS_{high}, and site OS corresponds to the outer-sphere ions.

Table 1: Positions and Energies of Adsorbed Strontium and Barium derived from the CMD metadynamics simulations.

Adsorbed Position	Strontium		Barium	
	d_{barite} (Å)	$\Delta G_{adsorption}$ (kJ/mol)	d_{barite} (Å)	$\Delta G_{adsorption}$ (kJ/mol)
IS_{low}	2.4	-15	2.6	-34
IS_{high}	3.5	-10	3.6	-21
IS_{NB}	3.6	-14	3.7	-21
OS	6.3	-7	6.3	-2

* d_{barite} is defined as the distance to the average position of the first layer of bariums in barite. ** $\Delta G_{adsorption}$ is the free energy relative to the dissolved ion.

Table 2: Positions and Relative Energies of Adsorbed Strontium from CMD optimized DFT and DFT simulations for qualitative comparison with the XR derived positions. Energies are relative to the inner-sphere adsorbed ion model (z = 2.2 Å).

Sr Position	z (Å)	PE (kJ/mol) F3C Model	PE (kJ/mol) SPC/E Model	DFT results
Outer-Sphere	4.8	+78	+148	+50
Sr^{2+}-Cl^- ion pair	1	+48	+83	+43*
Ba_{low}	-1.1	+71	+91	-6
Ba_{high}	0	+40	+111	+8

* - Note that the Sr^{2+}-Cl^- ion pair constrained the Sr^{2+} position to approximately 1 Å above the surface to mimic the peak of the RAXR data.

References

1. Smith, K. S. Metal sorption on mineral surfaces: an overview with examples relating to mineral deposits. In *The Environmental Geochemistry of Mineral Deposits, Part A. Processes, Techniques, and Health Issues*, Plumlee, G. S. L., M.J., Ed. Society of Economic Geologists: Littleton, CO, 1999; Vol. Rev. Econ. Geol. 6A, pp 161–182.
2. Sverjensky, D. A. Physical surface-complexation models for sorption at the mineral-water interface. *Nature* **1993,** *364*, 776-780.
3. Stumm W.; Morgan, J. J. *Aquatic Chemistry: Chemical Equilibria and Rates in Natural Waters*. 3rd ed.; John Wiley and Sons, Inc.: New York, 1996.
4. Hiemstra, T.; Van Riemsdijk, W. H. On the relationship between charge distribution, surface hydration, and the structure of the interface of metal hydroxides. *J. Colloid Interface Sci.* **2006,** *301*, 1-18.
5. Hiemstra, T.; VanRiemsdijk, W. H. A surface structural approach to ion adsorption: The charge distribution (CD) model. *J. Colloid Interface Sci.* **1996,** *179*, 488-508.
6. Hiemstra, T.; Venema, P.; VanRiemsdijk, W. H. Intrinsic proton affinity of reactive surface groups of metal (hydr)oxides: The bond valence principle. *J. Colloid Interface Sci.* **1996,** *184*, 680-692.
7. Lee, S. S.; Fenter, P.; Park, C.; Sturchio, N. C.; Nagy, K. L. Hydrated cation speciation at the muscovite (001)-water interface. *Langmuir* **2010,** *26*, 16647-16651.
8. Catalano, J. G.; Park, C.; Fenter, P.; Zhang, Z. Simultaneous inner- and outer-sphere arsenate adsorption on corundum and hematite. *Geochim. Cosmochim. Acta* **2008,** *72*, 1986-2004.
9. Noerpel, M. R.; Lee, S. S.; Lenhart, J. J. X-ray analyses of lead adsorption on the (001), (110), and (012) hematite surfaces. *Environ. Sci. Technol.* **2016,** *50*, 12283-12291.
10. Bellucci, F.; Lee, S. S.; Kubicki, J. D.; Bandura, A.; Zhang, Z.; Wesolowski, D. J.; Fenter, P. Rb^+ adsorption at the quartz(101)-aqueous interface: Comparison of resonant anomalous x-ray reflectivity with ab initio calculations. *J. Phys. Chem. C* **2015,** *119*, 4778-4788.
11. Lee, S. S.; Fenter, P.; Nagy, K. L.; Sturchio, N. C. Real-time observation of cation exchange kinetics and dynamics at the muscovite-water interface. *Nat. Commun.* **2017,** *8*, 15826.

12. Lee, S. S.; Fenter, P.; Nagy, K. L.; Sturchio, N. C. Changes in adsorption free energy and speciation during competitive adsorption between monovalent cations at the muscovite (001)-water interface. *Geochim. Cosmochim. Acta* **2013,** *123*, 416-426.
13. Lee, S. S.; Fenter, P.; Nagy, K. L.; Sturchio, N. C. Monovalent ion adsorption at the muscovite (001)-solution interface: Relationships among ion coverage and speciation, interfacial water structure, and substrate relaxation. *Langmuir* **2012,** *28*, 8637-8650.
14. Zhang, Z.; Fenter, P.; Cheng, L.; Sturchio, N. C.; Bedzyk, M. J.; Predota, M.; Bandura, A.; Kubicki, J. D.; Lvov, S. N.; Cummings, P. T.; et al. Ion adsorption at the rutile-water interface: Linking molecular and macroscopic properties. *Langmuir* **2004,** *20*, 4954-4969.
15. Ridley, M. K.; Hiemstra, T.; van Riemsdijk, W. H.; Machesky, M. L. Inner-sphere complexation of cations at the rutile-water interface: A concise surface structural interpretation with the CD and MUSIC model. *Geochim. Cosmochim. Acta* **2009,** *73*, 1841-1856.
16. Machesky, M. L.; Predota, M.; Wesolowski, D. J.; Vlcek, L.; Cummings, P. T.; Rosenqvist, J.; Ridley, M. K.; Kubicki, J. D.; Bandura, A. V.; Kumar, N.; et al. Surface protonation at the rutile (110) interface: Explicit incorporation of solvation structure within the refined MUSIC model framework. *Langmuir* **2008,** *24*, 12331-12339.
17. Villegas-Jimenez, A.; Mucci, A.; Paquette, J. Proton/calcium ion exchange behavior of calcite. *Phys. Chem. Chem. Phys.* **2009,** *11*, 8895-8912.
18. Villegas-Jimenez, A.; Mucci, A.; Pokrovsky, O. S.; Schott, J. Defining reactive sites on hydrated mineral surfaces: Rhombohedral carbonate minerals. *Geochim. Cosmochim. Acta* **2009,** *73*, 4326-4345.
19. Stipp, S. L. S. Toward a conceptual model of the calcite surface: Hydration, hydrolysis, and surface potential. *Geochim. Cosmochim. Acta* **1999,** *63*, 3121-3131.
20. Heberling, F.; Trainor, T. P.; Luetzenkirchen, J.; Eng, P.; Denecke, M. A.; Bosbach, D. Structure and reactivity of the calcite-water interface. *J. Colloid Interface Sci.* **2011,** *354*, 843-857.
21. Lee, S. S.; Heberling, F.; Sturchio, N. C.; Eng, P. J.; Fenter, P. Surface charge of the calcite (104) terrace measured by Rb^{+} adsorption in aqueous solutions using resonant anomalous x-ray reflectivity. *J. Phys. Chem. C* **2016,** *120*, 15216-15223.
22. Elzinga, E. J.; Rouff, A. A.; Reeder, R. J. The long-term fate of Cu^{2+}, Zn^{2+}, and Pb^{2+} adsorption complexes at the calcite surface: An x-ray absorption spectroscopy study. *Geochim. Cosmochim. Acta* **2006,** *70*, 2715-2725.

23. Rouff, A. A.; Elzinga, E. J.; Reeder, R. J.; Fisher, N. S. The influence of pH on the kinetics, reversibility and mechanisms of Pb(II) sorption at the calcite-water interface. *Geochim. Cosmochim. Acta* **2005,** *69*, 5173-5186.

24. Rouff, A. A.; Elzinga, E. J.; Reeder, R. J.; Fisher, N. S. X-ray absorption spectroscopic evidence for the formation of Pb(II) inner-sphere adsorption complexes and precipitates at the calcite-water interface. *Environ. Sci. Technol.* **2004,** *38*, 1700-1707.

25. Godelitsas, A.; Astilleros, J. M.; Hallam, K.; Harissopoulos, S.; Putnis, A. Interaction of calcium carbonates with lead in aqueous solutions. *Environ. Sci. Technol.* **2003,** *37*, 3351-3360.

26. Callagon, E.; Fenter, P.; Nagy, K. L.; Sturchio, N. C. Incorporation of Pb at the calcite (104)-water interface. *Environ. Sci. Technol.* **2014,** *48*, 9263-9269.

27. Wolthers, M.; Di Tommaso, D.; Du, Z.; de Leeuw, N. H. Calcite surface structure and reactivity: molecular dynamics simulations and macroscopic surface modelling of the calcite-water interface. *Phys. Chem. Chem. Phys.* **2012,** *14*, 15145-15157.

28. Hang, J. Z.; Zhang, Y. F.; Shi, L. Y.; Feng, X. Electrokinetic properties of barite nanoparticles suspensions in different electrolyte media. *J. Mater. Sci.* **2007,** *42*, 9611-9616.

29. Williams, H. Primary charging behavior and the interaction of calcium at the barite-water interface from 15 to 50˚C. B.S. Thesis, Texas Tech University, Lubbock, TX, 2016.

30. Sanchez-Pastor, N.; Pina, C. M.; Astilleros, J. M.; Fernandez-Diaz, L.; Putnis, A. Epitaxial growth of celestite on barite (001) face at a molecular scale. *Surf. Sci.* **2005,** *581*, 225-235.

31. YuHang, C.; Asenjo, A.; Sanchez-Pastor, N.; Fernandez-Diaz, L.; Gomez, J.; Pina, C. M. Growth of BaxSr1-xSO4 nano-steps on barite (001) face. *Surf. Sci.* **2007,** *601*, 381-389.

32. Weber, J. B., J.; Poplawsky, J.; Ievlev, A.; More, K.; Lorenz, M.; Bertagni, A.; Jindra, S.; Starchenko, V.; Higgins, S.; Stack, A. Unraveling the effects of strontium incorporation on barite growth – in-situ and ex-situ observations using multi-scale chemical imaging. *Cryst. Growth Des.* **2018,** *18*, 5521–5533.

33. Bracco, J. N.; Lee, S. S.; Stubbs, J. E.; Eng, P. J.; Heberling, F.; Fenter, P.; Stack, A. G. Hydration structure of the barite (001)-water interface: Comparison of x-ray reflectivity with molecular dynamics simulations. *J. Phys. Chem. C* **2017,** *121*, 12236-12248.

34. Bokern, D. G.; Hunter, K. A.; McGrath, K. M. Charged barite-aqueous solution interface: Surface potential and atomically resolved visualization. *Langmuir* **2003,** *19*, 10019-10027.

35. Collins, I. R., Surface electrical properties of barium sulfate modified by adsorption of poly

alpha, beta aspartic acid. *J. Colloid Interface Sci.* **1999,** *212*, 535-544.

36. Van Gusteren, W. F. B., S. R.; Eising, A. A.; Hunenberger, P. H.; Kruger, P. K. H. C.; Mark, A. E.; Scott, W. R.; Tironi, I. G. Biomolecular Simulation: The GROMOS96 manual and user guide. Hochschulverlag AG: Zurich, Switzerland, 1996.
37. Piana, S.; Jones, F.; Gale, J. D. Assisted desolvation as a key kinetic step for crystal growth. *J. Am. Chem. Soc.* **2006,** *128*, 13568-13574.
38. Jang, Y. H.; Chang, X. Y.; Blanco, M.; Hwang, S. G.; Tang, Y. C.; Shuler, P.; Goddard, W. A. The MSXX force field for the barium sulfate-water interface. *J. Phys. Chem. B* **2002,** *106*, 9951-9966.
39. Stack, A. G.; Raiteri, P.; Gale, J. D. Accurate rates of the complex mechanisms for growth and dissolution of minerals using a combination of rare-event theories. *J. Am. Chem. Soc.* **2012,** *134*, 11-14.
40. Bracco, J. N.; Gooijer, Y.; Higgins, S. R. Hydrothermal atomic force microscopy observations of barite step growth rates as a function of the aqueous barium-to-sulfate ratio. *Geochim. Cosmochim. Acta* **2016,** *183*, 1-13.
41. Fenter, P. A. X-ray reflectivity as a probe of mineral-fluid interfaces: A user guide. *Rev. Mineral. Geochem.* **2002**, 49, 149– 220.
42. Lee, S. S.; Fenter, P.; Park, C. Optimizing a flow-through X-ray transmission cell for studies of temporal and spatial variations of ion distributions at mineral-water interfaces. *J. Synchrotron Radiat.* **2013,** *20*, 125-136.
43. Robinson, I. K. Crystal truncation rods and surface roughness. *Phys. Rev. B* **1986,** *33*, 3830-3836.
44. Park, C.; Fenter, P. A. Phasing of resonant anomalous x-ray reflectivity spectra and direct Fourier synthesis of element-specific partial structures at buried interfaces. *J. Appl. Crystallogr.* **2007,** *40*, 290-301.
45. Cross, J. O.; Newville, M.; Rehr, J. J.; Sorensen, L. B.; Bouldin, C. E.; Watson, G.; Gouder, T.; Lander, G. H.; Bell, M. I. Inclusion of local structure effects in theoretical x-ray resonant scattering amplitudes using ab initio x-ray-absorption spectra calculations. *Phys. Rev. B* **1998,** *58*, 11215-11225.
46. Kresse, G.; Hafner, J. Ab-initio molecular-dynamics for open-shell transition-metals. *Phys. Rev. B* **1993,** *48*, 13115-13118.

47. Kresse, G.; Furthmuller, J.; Hafnerr, J. Theory of the crystal-structures of selenium and tellurium - The effect of generalized-gradient corrections to the local-density approximation. *Phys. Rev. B* **1994,** *50*, 13181-13185.

48. Kresse, G.; Hafner, J. Ab-initio molecular-dynamics simulation of the liquid-metal amorphous-semiconductor transition in germanium. *Phys. Rev. B* **1994,** *49*, 14251-14269.

49. Kresse, G.; Furthmuller, J. Efficient iterative schemes for ab initio total-energy calculations using a plane-wave basis set. *Phys. Rev. B* **1996,** *54*, 11169-11186.

50. Stack, A. G. Molecular dynamics simulations of solvation and kink site formation at the {001} barite-water interface. *J. Phys. Chem. C* **2009,** *113*, 2104-2110.

51. Stack, A. G.; Borreguero, J. M.; Prisk, T. R.; Mamontov, E.; Wang, H.-W.; Vlcek, L.; Wesolowski, D. J. Precise determination of water exchanges on a mineral surface. *Phys. Chem. Chem. Phys.* **2016,** *18*, 28819-28828.

52. Warren, D. M. Molecular dynamics simulation of barite and celestite ion-pairs. M.S. Thesis, Georgia Institute of Technology, Atlanta, GA, 2011.

53. Levitt, M.; Hirshberg, M.; Sharon, R.; Laidig, K. E.; Daggett, V. Calibration and testing of a water model for simulation of the molecular dynamics of proteins and nucleic acids in solution. *J. Phys. Chem. B* **1997,** *101*, 5051-5061.

54. Berendsen, H. J. C.; Grigera, J. R.; Straatsma, T. P. The missing term in effective pair potentials. *J. Phys. Chem.* **1987,** *91*, 6269-6271.

55. Laio, A.; Gervasio, F. L. Metadynamics: a method to simulate rare events and reconstruct the free energy in biophysics, chemistry and material science. *Rep. Prog. Phys.* **2008,** *71*, 126601.

56. Bonomi, M.; Branduardi, D.; Bussi, G.; Camilloni, C.; Provasi, D.; Raiteri, P.; Donadio, D.; Marinelli, F.; Pietrucci, F.; Broglia, R. A.; et al. PLUMED: A portable plugin for free-energy calculations with molecular dynamics. *Comput. Phys. Commun.* **2009,** *180*, 1961-1972.

57. Plimpton, S. Fast parallel algorithms for short-range molecular-dynamics. *J. Compu. Phys.* **1995,** *117*, 1-19.

58. Barducci, A.; Bussi, G.; Parrinello, M. Well-tempered metadynamics: A smoothly converging and tunable free-energy method. *Phys. Rev. Lett.* **2008,** *100*, 020603.

59. Raiteri, P.; Laio, A.; Gervasio, F. L.; Micheletti, C.; Parrinello, M. Efficient reconstruction of complex free energy landscapes by multiple walkers metadynamics. *J. Phys. Chem. B* **2006,** *110* (8), 3533-3539.

60. Childs, H. B., E.; Whitlock, B.; Meredith, J.; Ahern, J. Pugmire, D.; Biagas, K.; Miller, M.; Harrison, C.; Weber, G. H.; Krishnan H.; Fogal, T.; Sanderson, A.; et al. VisIt: An end-user tool for visualizing and analyzing very large data. In *High Performance Visualization--Enabling Extreme-Scale Scientific Insight*, CRCPress Boca Raton, 2012.

61. Jacobsen, S. D.; Smyth, J. R.; Swope, R. J.; Downs, R. T. Rigid-body character of the SO_4 groups in celestine, anglesite and barite. *Can. Mineral.* **1998,** *36*, 1053-1060.

62. Lee S. S.; Nagy K. L.; Park C.; Fenter P. Enhanced uptake and modified distribution of mercury(II) by fulvic acid on the muscovite (0 0 1) surface. *Environ. Sci. Technol.* **2009**, 43, 5295–5300.

63. Bockris, J. O.; Khan, S. U. M. *Surface electrochemistry: A molecular level approach*. 1 ed.; Springer: New York, 1993.

64. Stack, A. G.; Rustad, J. R. Structure and dynamics of water on aqueous barium ion and the {001} barite surface. *J. Phys. Chem. C* **2007,** *111*, 16387-16391.

65. Aqvist, J. Ion water interaction potentials derived from free-energy perturbation simulations. *J. Phys. Chem.* **1990,** *94*, 8021-8024.

66. Marcus, Y. *Ion Solvation*. John Wiley & Sons: London, 1985.

67. Pohorille, A.; Chipot, C. *Free Energy Calculations: Theory and Applications in Chemistry and Biology*. Springer-Verlag: Berlin, 2007.

68. Persson, I.; Sandstrom, M.; Yokoyama, H.; Chaudhry, M. Structure of the solvated strontium and barium ions in aqeous, dimethyl-sulfoxide and pyridine solution, and crystal structure of the strontium andbarium hydroxide octahydrate. *Zeitschrift Fur Naturforschung Section a-a Journal of Physical Sciences* **1995,** *50*, 21-37.

69. Dove, P. M.; Czank, C. A. Crystal-chemical controls on the dissolution kinetics of the isostructural sulfates- Celestite, anglesite, and barite. *Geochim. Cosmochim. Acta* **1995,** *59*, 1907-1915.

70. Felmy, A. R.; Rai, D.; Amonette, J. E. The solubility of barite and celestite in sodium-sulfate - Evaluation of thermodynamic data. *J. Solution Chem.* **1990,** *19*, 175-185.

71. Godelitsas, A.; Astilleros, J. M.; Hallam, K. R.; Lons, J.; Putnis, A. Microscopic and spectroscopic investigation of the calcite surface interacted with Hg(II) in aqueous solutions. *Mineral. Mag.* **2003,** *67*, 1193-1204.

72. Catelani, T.; Perito, B.; Bellucci, F.; Lee, S. S.; Fenter, P.; Newville, M.; Rimondi, V.; Pratesi, G.; Costagliola, P. Arsenic uptake in bacterial calcite. *Geochim. Cosmochim. Acta* **2018,** *222*, 642-654.

73. Callagon, E. B. R.; Lee, S. S.; Eng, P. J.; Laanait, N.; Sturchio, N. C.; Nagy, K. L.; Fenter, P. Heteroepitaxial growth of cadmium carbonate at dolomite and calcite surfaces: Mechanisms and rates. *Geochim. Cosmochim. Acta* **2017,** *205*, 360-380.

74. Baes, C. F.; Mesmer, B E. *The Hydrolysis of Cations*. Krieger Publishing Group: Malabar, Florida, 1976.

75. Weber, J.; Barthel, J.; Klinkenberg, M.; Bosbach, D.; Kruth, M.; Brandt, F. Retention of Ra-226 by barite: The role of internal porosity. *Chem. Geol.* **2017,** *466*, 722-732.

TOC Graphic